Oral presentation | Turbulent flow

Turbulent flow-II

Wed. Jul 17, 2024 10:45 AM - 12:45 PM Room B

[7-B-02] Machine Learning Categorization of a Large CFD Data Set of Airfoil Leading-Edge Defects

*Andre F. P. Ribeiro[1], Alexander Meyer Forsting[2] （1. Delft University of Technology, 2. Technical University of Denmark）

Keywords: Wind Turbines, Erosion, Artificial Neural Networks

Twelfth International Conference on Computational Fluid Dynamics (ICCFD12), Kobe, Japan, July 14-19, 2024

Machine Learning Categorization of a Large CFD Data Set of Airfoil Leading-Edge Defects

A.F.P. Ribeiro* and A. Meyer Forsting**
Corresponding author: A.PintoRibeiro@tudelft.nl
* Delft University of Technology, Netherlands.
** Technical University of Denmark, Denmark.

Abstract: Leading edge (LE) defects and damages on wind turbine blades are a significant cost driver within the wind industry, as they endanger the blades' structural integrity whilst also diminishing their aerodynamic performance. While the structural integrity of the blades is paramount and must be accounted for when performing damage diagnosis, the aerodynamic effects of LE defects can lead to significant production losses, providing a financial incentive for carrying out repairs. Yet to evaluate those aerodynamic losses, first damages need to be identified in blade inspection images and then be grouped by their severity. Currently there is no procedure for performing such grouping or categorization in terms of aerodynamic impact, though. Hence in this work we analyze a recently generated 2D-CFD database of airfoil polars with 11 different types of LE defects to establish how they could potentially be grouped. By visualizing the data and using artificial neural networks, we conclude that many types of defects can be categorized simply by their distance to the LE. This can help decision making on blade maintenance with drone-based imagery. Other defects, such as changes to the airfoil camber behave substantially different and require their own categories.

Keywords: wind turbine, erosion, artificial neural networks.

1 Introduction

Leading edge (LE) defects/damages on wind turbine blades are a significant cost driver within the wind industry, as they endanger the blades' structural integrity whilst also diminishing their aerodynamic performance [1, 2, 3]. This has made LE erosion research more common in recent years [4, 5], including efforts to model erosion effects computationally [6]. Whilst larger turbines produce power at lower cost, they are also more likely to suffer from LE erosion damage, as their blade tips are striking airborne particles (rain, hail, sand etc.) at greater speed [7], thus this issue — despite some promising mitigation strategies being deployed — is going to remain. Turbines are regularly inspected to ensure their optimal operation and schedule maintenance procedures. This includes image-based reports detailing each blade's condition, nowadays often performed by drones carrying high resolution cameras. Ideally, those images could be automatically processed to identify defects and help making informed maintenance decisions. Whilst under structural considerations particularly cracks in the laminate are flagged, even small, structurally insignificant, surface perturbations (in the order of 0.1mm) can be significant aerodynamically [8, 9, 10], especially as modern turbines blades operate at Reynolds numbers well above 10 million. This is especially true for the flow around the LE, where the boundary layer is thin and is experiencing strong acceleration.

As the appearance of LE surface perturbations is a product of interacting stochastic factors, including the material composition, environmental conditions, and production process, its geometric manifestation is equally stochastic and thus highly varied. Hence, countless possible LE defect types with equally many parametric variations could be conceived, making it difficult to match observed damages from drone-based imagery to a particular type and associate it with a certain aerodynamic loss, which would then help determining whether a repair would financially make sense. To facilitate the conversion from inspection imagery to aerodynamic losses it would thus be beneficial to group all types and manifestations of damages/defects into certain severity classes and connect them to certain damage parameters, like location or size for instance. Images could then specifically be searched for those particular features and categorized accordingly by an algorithm.

A deep numerical investigation using 2D Reynolds averaged Navier-Stokes (RANS) simulations on the effects of leading-edge (LE) defects on airfoil aerodynamics was recently conducted [11] that parameterized 11 forms of commonly observed LE surface imperfections and computed their impact on performance. The generated aerodynamic data set is openly-available and investigated here [12] to unearth certain correlations between the many damage types and evaluate if they can be grouped.

In this work, we seek to explore the aforementioned LE defect data set and understand the aerodynamic effects of each of the defect types. Then, using artificial neural networks [13] (NN), we verify if the aerodynamic penalties of LE defects can be used to find which type of defect is present. With these two steps concluded, we attempt to define a new classification for LE defects, based on aerodynamics effects and geometry properties of the defects themselves.

2 The data set

We utilize the aerodynamic properties computed for all 2868 parametric defects variations within the CFD database [11] under the transitional boundary layer regime. We exclude the fully turbulent cases as they are much less sensitive to LE defects. We also exclude the defects related to roughness, as they were modeled using modifications to fully turbulent boundary layers [14]. The defect types and their variables are shown in Fig. 1 (the filled overhang is not shown, but corresponds to removing the step of the overhang by attaching a curve smoothly to the surface) and listed in Table 1.

Defect	Variable 1	Variable 2	Variable 3
Overhang	height (h)	-	-
Filled overhang	height (h)	-	-
Vertical LE translation	displacement (Δy)	-	-
Stall strip	distance to LE (s)	height (h)	-
Flat patch	distance to LE (s)	width (Δs)	-
Waviness	amplitude (h)	wavelength (λ)	-
Symmetric loss/addition	width (Δs)	height (h)	-
Slot	height (h)	distance to LE (s)	width (Δs)
Backward facing step	height (h)	distance to LE (s)	width (Δs)
Forward facing step	height (h)	distance to LE (s)	width (Δs)

Table 1: Types of defects and their variables.

The data set includes lift (C_l) and drag (C_d) polars for various Reynolds numbers (Re), along with integral quantities associated with the said polars. From these integral values we select the aerodynamic parameters that we analyze for each of the defects. These integral aerodynamic parameters include a combination of the minimum or maximum values of C_l, C_d, and their ratio, along with the angle of attack (α) associated with such values. While $\max(C_l)$ is a useful parameter that is very sensitive to the airfoil geometry, its accuracy when obtained from a 2D RANS simulation is questionable at best. On the other hand, $\max(C_l/C_d)$ tends to occur before stall and can be obtained reliably. The fact that the data set is 2D also means that 3D effects from sections very close to the blade tips are neglected. Table 2 summarizes the integral aerodynamic effects chosen for the studies conducted here.

Parameter	Description
$\Delta\max(C_l/C_d)$	Change in maximum lift over drag
$\Delta\alpha@\max(C_l/C_d)$	Change in angle of attack for maximum lift over drag [°]
$\Delta C_l(\alpha=0°)$	Change in lift coefficient at zero angle of attack
$\Delta\alpha@C_l=0$	Change in angle of attack for zero lift [°]
$\Delta\min(C_d)$	Change in minimum drag coefficient
$\Delta\alpha@\min(C_d)$	Change in angle of attack at minimum drag [°]

Table 2: Integral aerodynamic parameters investigated.

Each aerodynamic parameter is plotted against all others in Fig. 2. Some separation of the different defects can be seen, but they are not clearly split into separate clusters. Hence, a determining which parameters are linked to which defects is a non-trivial task.

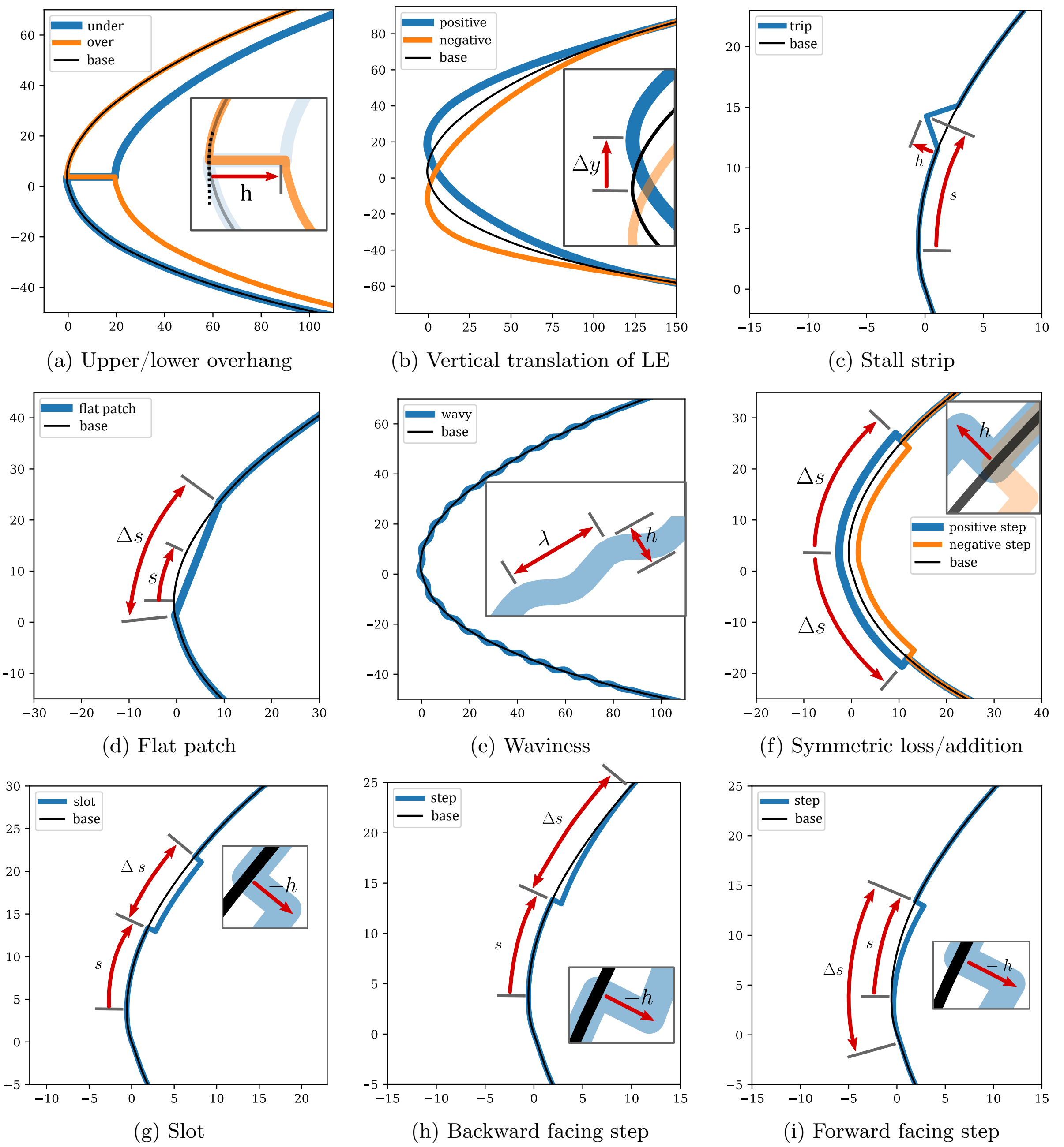

(a) Upper/lower overhang (b) Vertical translation of LE (c) Stall strip

(d) Flat patch (e) Waviness (f) Symmetric loss/addition

(g) Slot (h) Backward facing step (i) Forward facing step

Figure 1: Definitions of idealized damage and repair features. All dimensions are in thousands of chord length.

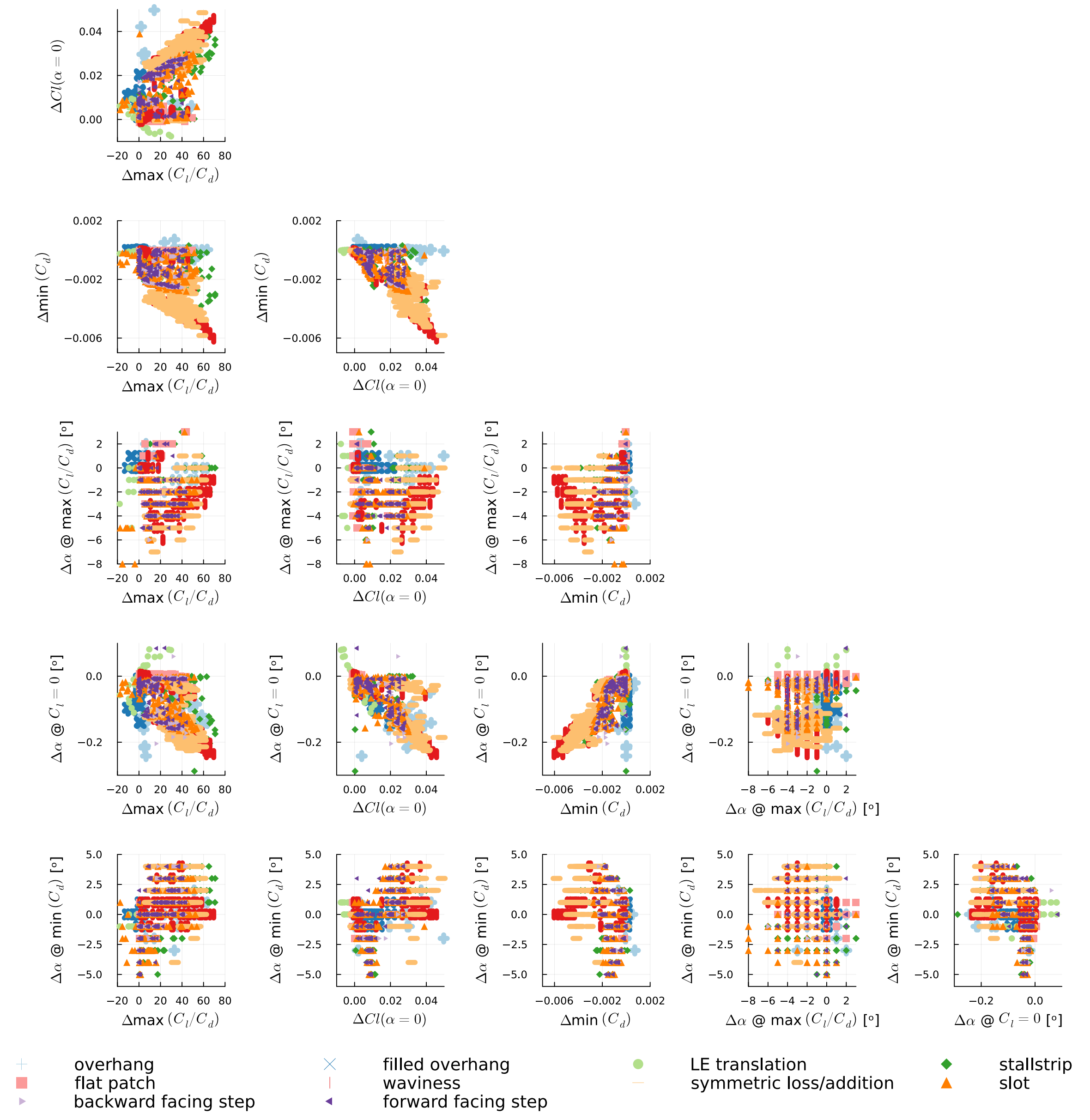

Figure 2: Scatter plots for all selected parameters, colored by defect type. Transitional cases only, $\mathrm{Re} = [3, 5, 10]$ million.

3 Defect effects on integral aerodynamic properties

3.1 Single variable defects

Throughout this section we show the effects of single variable defects on the integral aerodynamic characteristics. All values of Re in the data set are shown using different line types, although Re effects tend to be small.

In Fig. 3 we show the effects of overhang. Throughout the work, some outliers appeared in the data set, as the discontinuities around overhang heights of zero. These are due to numerical issues and can be ignored. We did not remove them from the dataset, as the number of outliers is generally low. The overhang can lead to large changes in most parameters. Note that $\Delta\alpha@C_l=0$ and $\Delta\alpha@\min(C_d)$ have a precision of 1° in the data set, which explains their irregular behaviors.

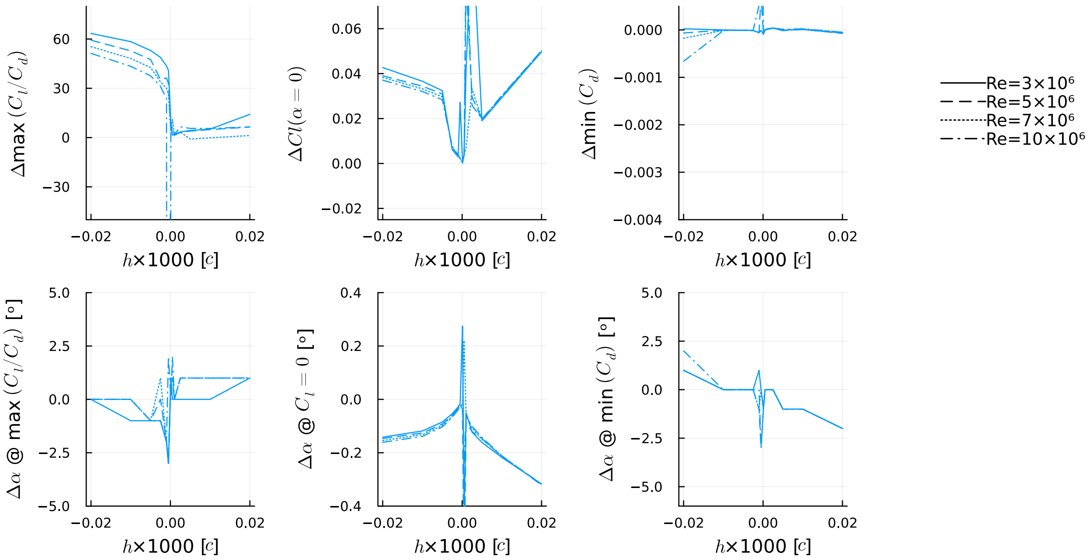

Figure 3: Overhang effects on aerodynamic parameters.

In Fig. 4 we show the effects of the filled overhang. Its effect on the aerodynamic parameters are limited compared to the other defects, as it represents a subtle change in the LE shape, instead of a discontinuity.

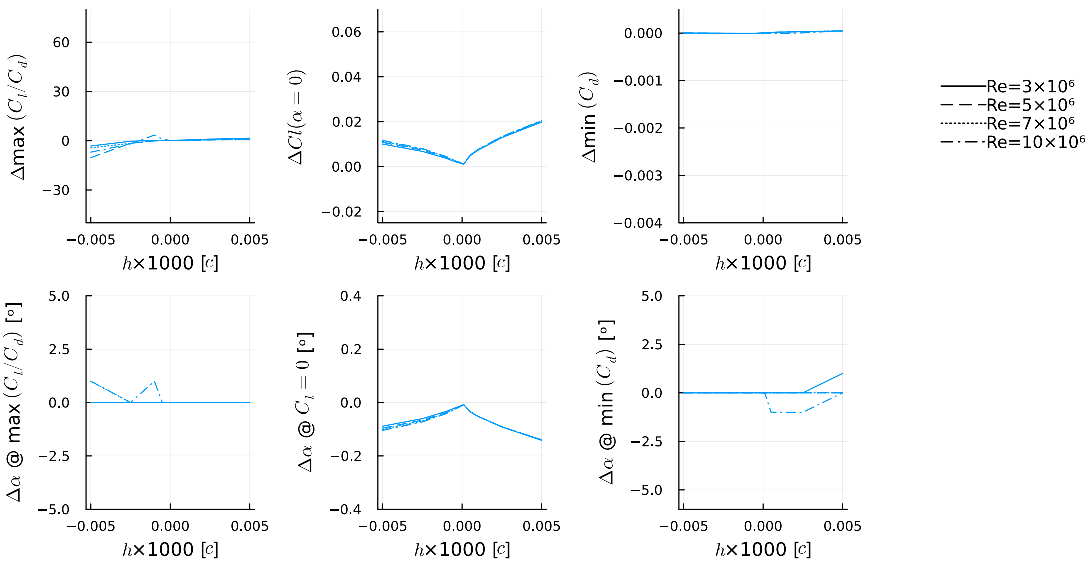

Figure 4: Filled overhang effects on aerodynamic parameters.

In Fig. 5 we show the effects of the LE translation, measured by the vertical distance Δy that the LE is translated. The translation changes the camber of the airfoil and can lead to negative $\Delta\max(C_l/C_d)$, meaning it can improve the airfoil efficiency. It seems to be the only defect that leads to a positive $\Delta\alpha @ C_l = 0$.

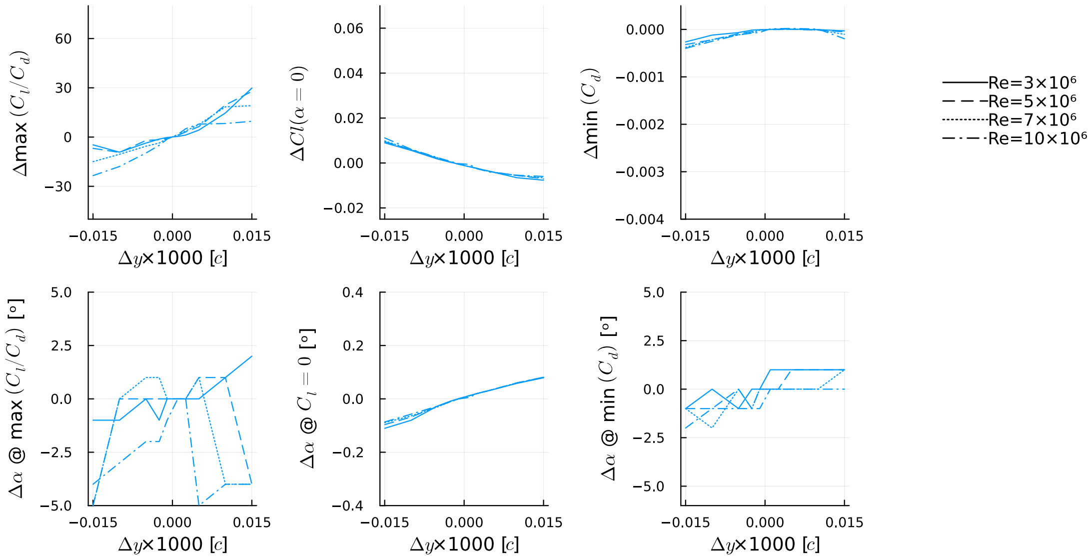

Figure 5: LE translation effects on aerodynamic parameters.

3.2 Two variable defects

We now focus on defects with two variables. Here we use the line colors to show the second variables, which tend to be much more effective in changing the aerodynamics than Re. The choice of which variable goes on the horizontal axis matters and can make visualization more or less clear. Hence, we do not always use the convention in Table 1 to select the first variable (on the horizontal axis) and the second variable (line colors).

In Fig. 6 we show the effects of the stall strip. Results are fairly insensitive to Re. The aerodynamic parameters vary substantially and nearly monotonically with the strip height h (colors) and the position s seems to split results into two groups: positive (suction side) and negative (pressure side) strip positions, with positive values of s leading to overall larger changes in aerodynamics.

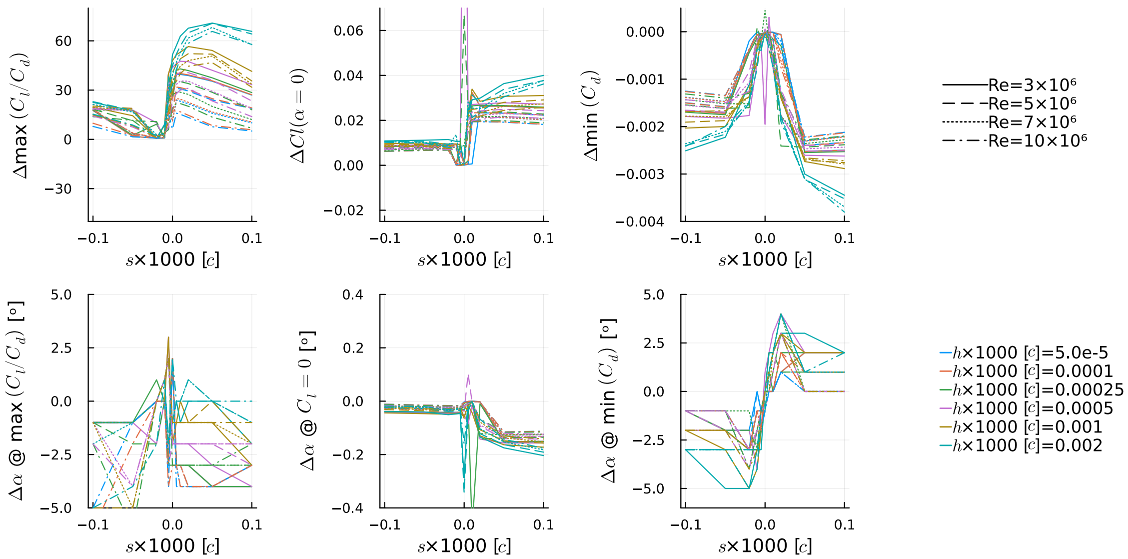

Figure 6: Stall strip effects on aerodynamic parameters.

In Fig. 7 we show the effects of the flat patch. It shows large positive $\Delta\max(C_l/C_d)$, with almost no change to many of the other parameters. The width Δs of the flat patch increases the aerodynamic effects nearly monotonically. It shows higher sensitivity when the flat patch is very close to the LE ($s \approx 0$), which is consistent, since the LE is the region of the airfoil with higher curvature, hence the region that is most modified when flattened.

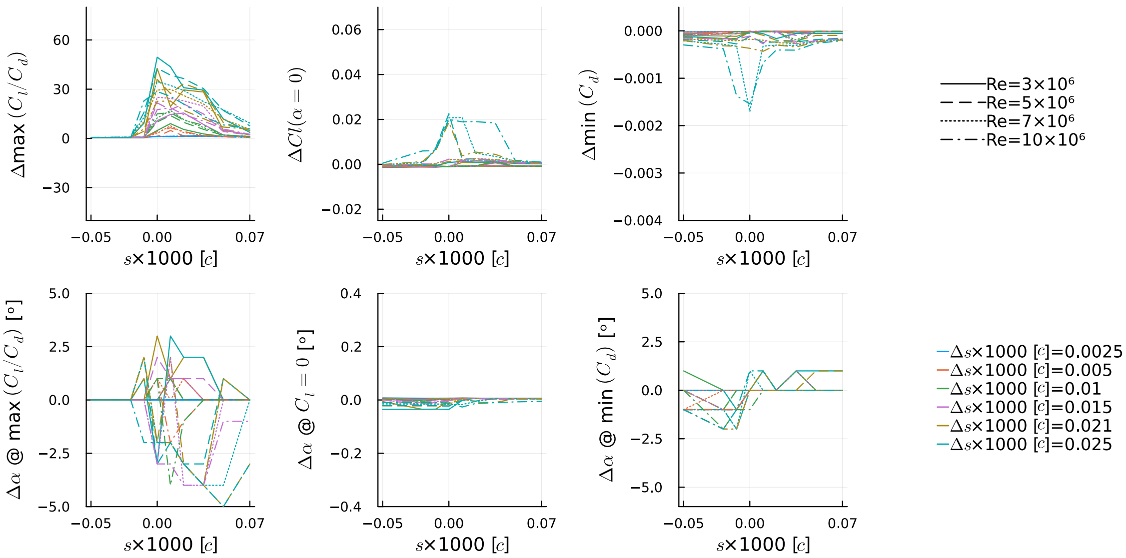

Figure 7: Flat patch effects on aerodynamic parameters.

In Fig. 8 we show the effects of waviness. It shows patterns in the parameters that are very similar to the stall strip, but leading to even larger deviations than seen in Fig. 6. While the amplitude h tends to have a clear and strong monotonic effect on the aerodynamics, the wavelength λ plays a smaller role.

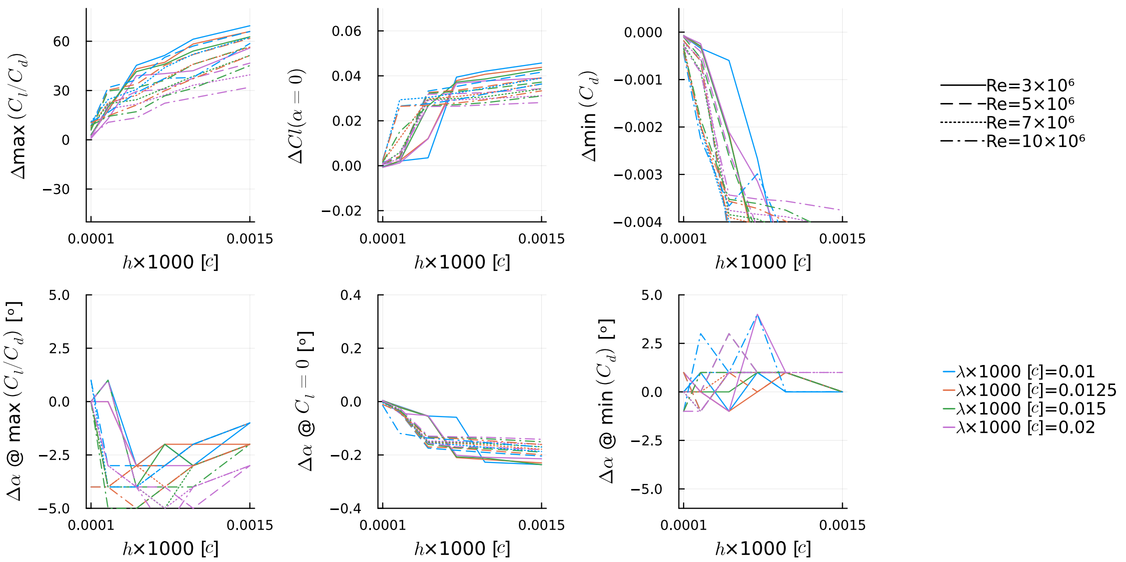

Figure 8: Waviness effects on aerodynamic parameters.

In Fig. 9 we show the effects of symmetric loss/addition. The effects are quite similar to waviness and the reasons why will be explored later in the paper. Again, the width Δs plays a smaller role than the height.

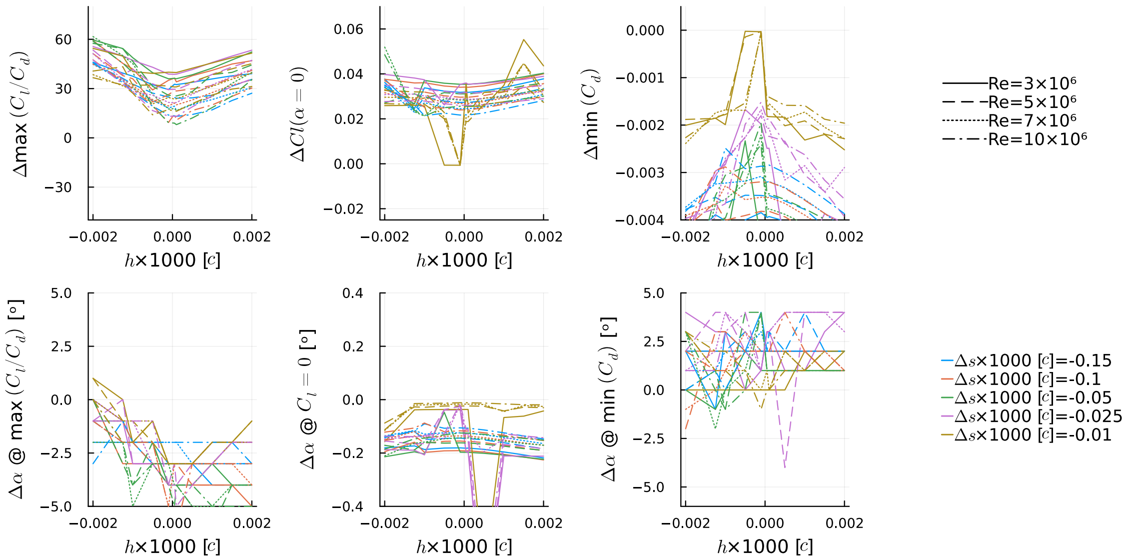

Figure 9: Symmetric loss/addition effects on aerodynamic parameters.

3.3 Three variable defects

Here we use the line thickness to show the third variables, which is the width of the affected area Δs for all defects. Colors are always the defect height h and the horizontal axis is always the position or distance s, relative to the LE. Again, the choice of which variable goes on the horizontal axis matters and the choices were made for clarity.

In Fig. 10 we show the effects of the slot, in Fig. 11 the effects of backward facing steps, and in Fig. 12 the effects of forward facing steps. All defects here behave in very similar ways, which is also remarkably similar to the stall strip. These similarities will be further clarified in later sections.

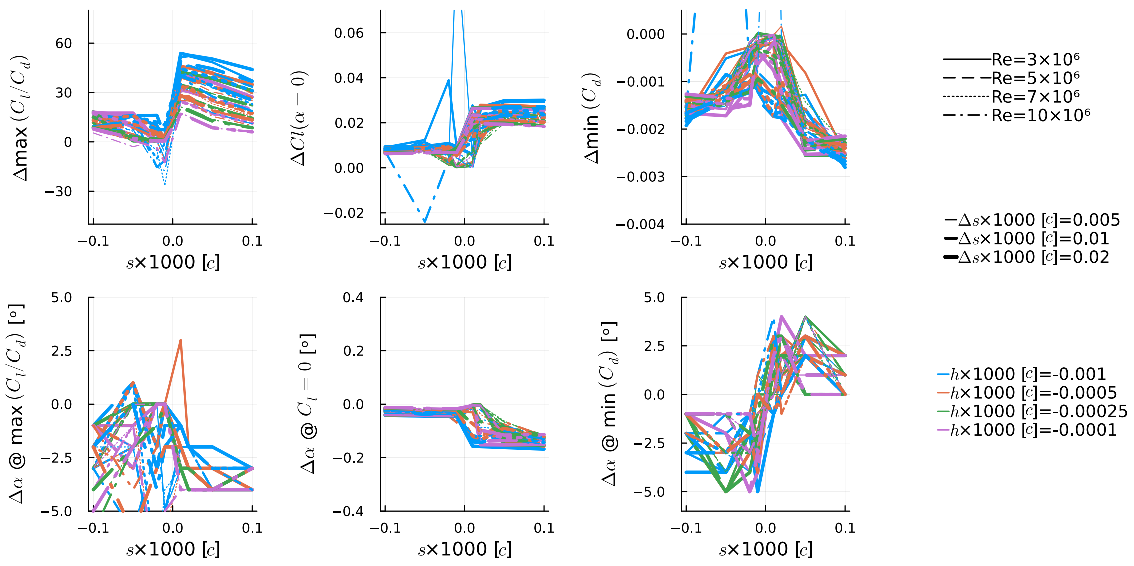

Figure 10: Slot effects on aerodynamic parameters.

4 Defects effects on local surface properties

The original data set used in this work only contains integral aerodynamic parameters. However, more information can be extracted from the simulations used to produce the data set. In this section, we plot for each defect type a number of curves representing the range of effects seen from looking at all the

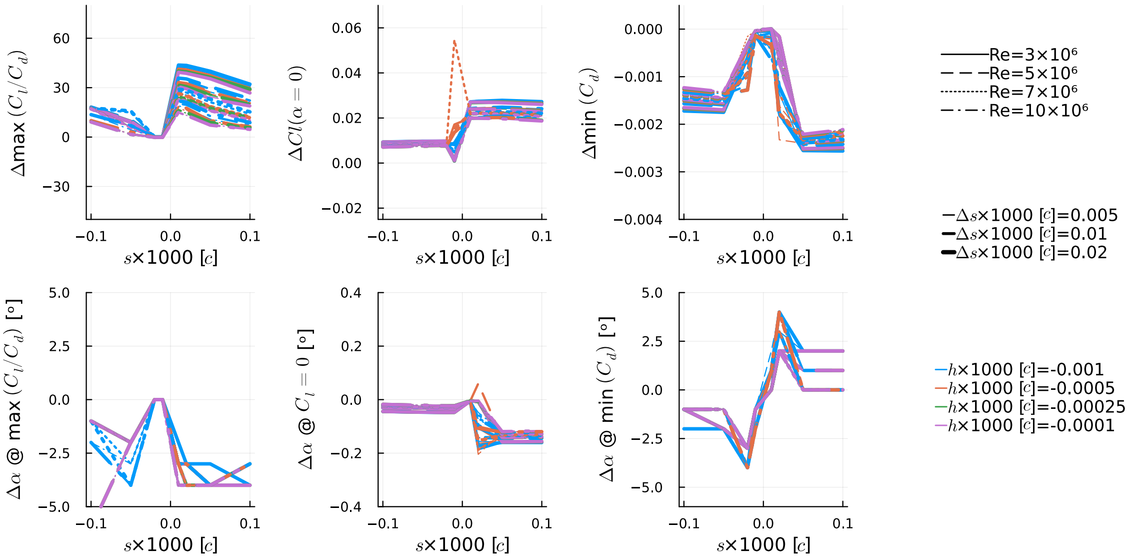

Figure 11: Backward facing step effects on aerodynamic parameters.

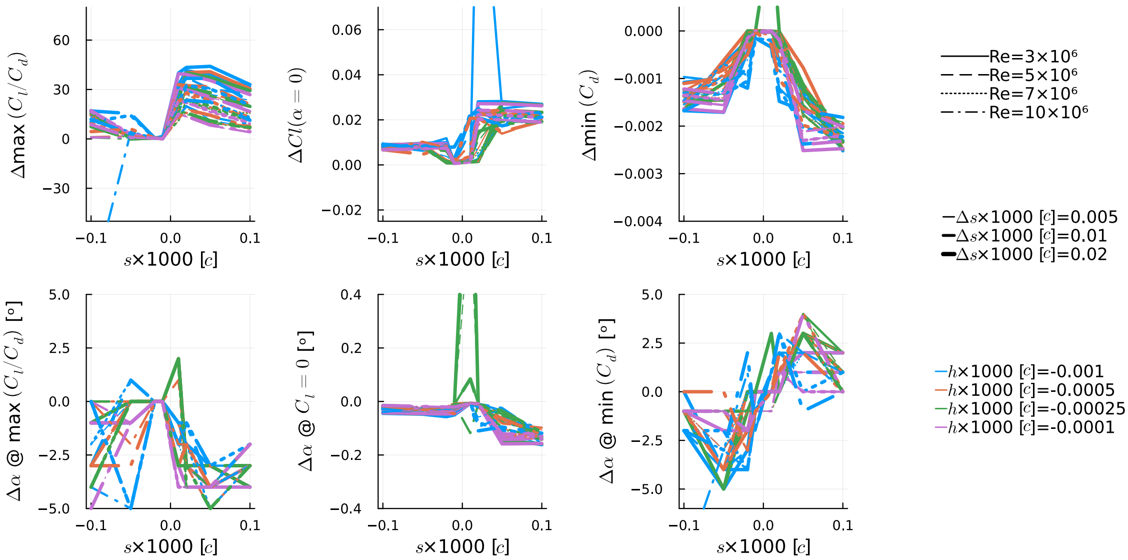

Figure 12: Forward facing step effects on aerodynamic parameters.

simulation results. We focus on $\mathrm{Re} = 3$ million and $\alpha = 7°$. We do this for clarity, as including all the simulation results makes the plots difficult to interpret. We use pressure coefficient $Cp = (p - p_\infty)/q_\infty$ and skin friction coefficient $Cf = \tau/q_\infty$ for our comparisons, where p is the static pressure on the airfoil surface, p_∞ is the freestream static pressure, q_∞ is the freestream dynamic pressure, and τ is the friction force on the airfoil surface. We analyze these results along the horizontal axis x, with coordinates normalized by the airfoil chord c.

The Cp and Cf distributions for the various defect types confirm some of the findings in the previous sections. Other than some edge cases leading to flow separation, the overhang, stall strip, symmetric loss/addition, slot, backward facing step, and forward facing steps behave in very similar ways. They all cause local peaks and dips in Cp, while triggering an early transition, seen by the earlier rise in Cf. Depending on the location of these defects, the transition can occur on either the suction or the pressure side of the airfoil, or in cases with two discontinuities (symmetric loss/addition and slot), both sides can transition earlier than the baseline. For some extreme cases, the steps can lead to separation bubbles on the suction side, but not on the pressure side. The filled overhang has minor effects on Cp and Cf, consistent with the small effects on integral parameters. The LE translation has the largest effect on Cp, with minor effects on Cf. It is also the only defect capable of delaying transition. The flat patch seems to function mostly as a transition trip, with smaller effect on Cp compared to the steps. Waviness is difficult to interpret, as the effect on both Cp and Cf is to cause small wavelength fluctuations. It can also lead to early transition, although only above a certain amplitude, which is consistent with the integral aerodynamic effects, which are negligible for small amplitudes. Similar to the symmetric loss/addition, waviness affects both pressure and suction sides concurrently. At this angle of attack, most defects only affect the suction side of the airfoil, causing earlier transition and small fluctuations in Cp.

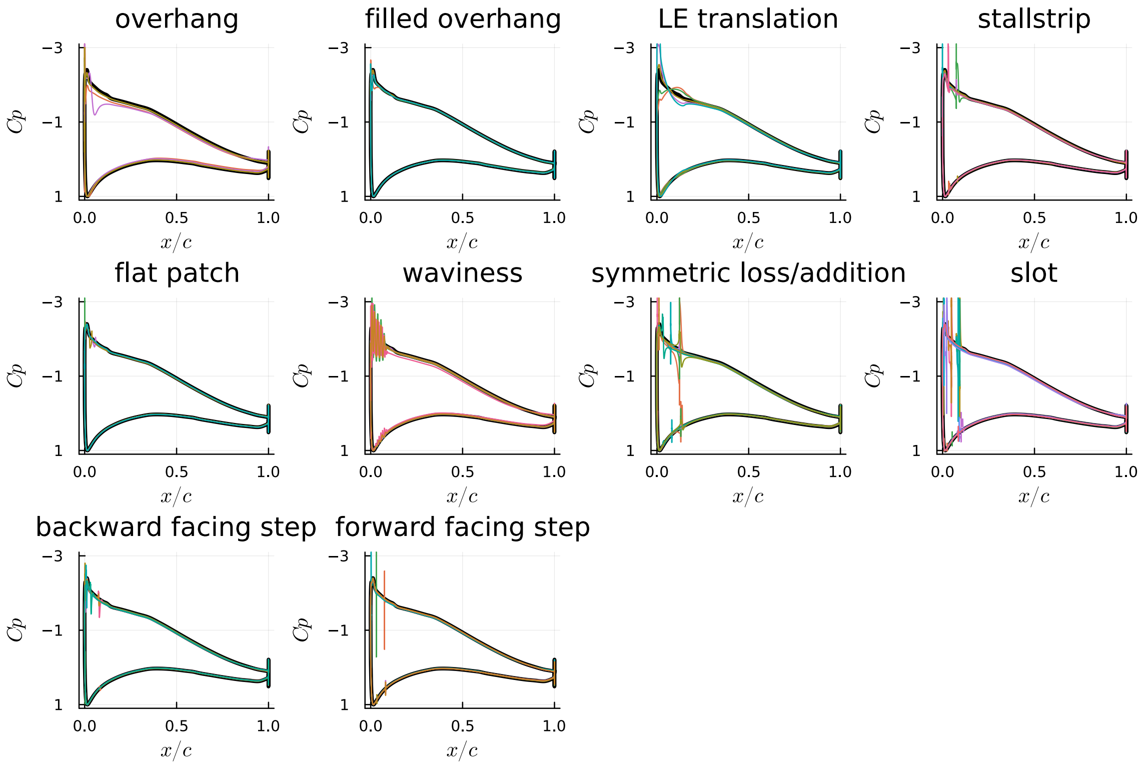

Figure 13: Pressure coefficient from representative simulations for the different defect types. Baseline results in black.

One conclusion from examining the Cp and Cf cuts is how difficult it is to differentiate most LE defects from visual interpretation of the aerodynamics alone. The Cp distribution after $x/c = 0.25$ seems almost entirely insensitive to the defects.

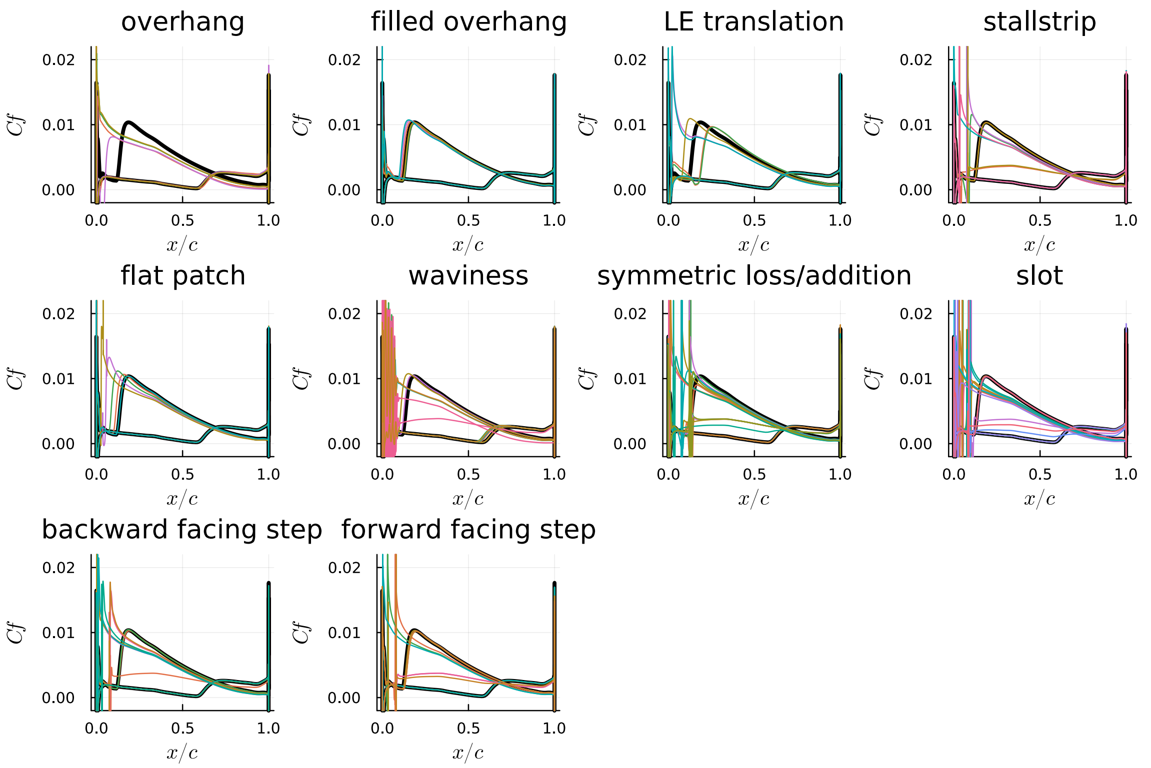

Figure 14: Skin friction coefficient from representative simulations for the different defect types. Baseline results in black.

5 Classification using machine learning

We now seek to understand if one can reverse the problem and identify from the aerodynamic parameters what the defects are. This servers the purpose to understand if the defects lead to different aerodynamic behaviors, or if they are equivalent. We formulate the problem here as a classification problem and use a NN where the six aerodynamic parameters acts as inputs and the ten defect types as outputs. NN have been successfully used to model from airfoil aerodynamics (e.g. [15]) to wind farm performance [16], including modelling LE defect effects on the cost of energy [17]. We choose not to use *Cp* and *Cf* as inputs because they are mostly sensitive to the defects near the LE, where their values can be very irregular. This makes it difficult to choose a specific x/c where *Cp* is measured and very difficult to use peak values. From a data interpolation standpoint, using Re as one of the inputs would facilitate the process. However, here we limit ourselves to the aerodynamic parameters as the only inputs to the NN.

5.1 Testing the model for different Reynolds numbers

We train the network with the data set for $\mathrm{Re} = [3, 5, 10]$ million and then test the network with the data set values for $\mathrm{Re} = 7$ million. We optimize the network size based on the training data. From running tests with one to three hidden layers, each with six to twenty neurons, the optimum setup was found to be one hidden layer with 19 neurons. This configuration led to the highest arithmetic and harmonic averages over all defects for correct predictions per number of cases.

We start by looking at the number of correct predictions by the NN. This is shown in Fig. 15. The filled overhang seems very easy to detect. The flat patch also has a high success rate. However, most defects seem to be detected correctly less than half of the time, while a few (waviness and overhang) are misdiagnosed for the vast majority of cases. Overall, the NN has trouble categorizing the data set. The difficulty in telling defects apart is investigated next.

In order to understand which defects are more similar to each other, according to the NN, we use the heatmap in Fig. 16. Each line shows a certain defect case. Each column is colored by the average result for each defect, as predicted by the NN. If the NN is perfect, then the diagonal will be one and all other elements zero. Here we can see which defects are more similar to each other, according to the NN. As a noteworthy example, for the filled overhang the NN can accurately predict the defect without false

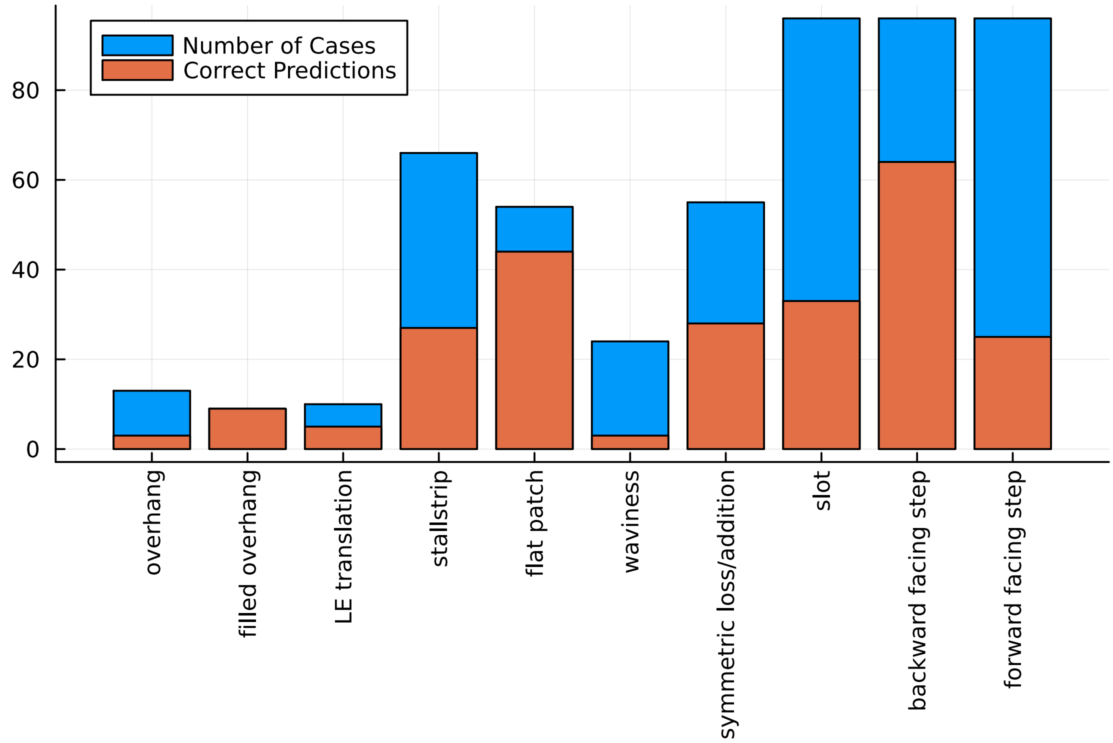

Figure 15: Number of cases and correct predictions using the NN, per defect type.

positives, but for LE translation, the NN can predict a possibility that it is a filled overhang. This is consistent with the fact that both defects involve making subtle changes to the LE curvature. Another point to highlight is that cases with symmetric loss/addition trigger waviness as output. As seen in Cf, both these types of defects lead to effects on both the suction and pressure sides of the airfoil.

The most obvious outcome of this analysis is that the stall strip is very often detected as other defects and vice-versa. Overhang, stall strip, symmetric loss/addition, backward facing step, and forward facing steps are all very similar in nature, being some sort of bump in the geometry that lead to early transition and potentially small separation zones. Hence, Fig. 16 confirms what was intuitively and visually inferred from the previous sections: these defects can all be grouped together from an aerodynamic standpoint.

The cases that the NN seems to distinguish quite well (over 45% of the time) are filled overhang, LE translation, and flat patch. As waviness is a distributed defect, geometrically quite distinct from the other defects, we will attempt to keep it in the next sections. All other defects can be grouped into a single group. However, as we have seen in the previous sections, symmetric loss/addition has some special features which we will address in the next sections.

5.2 Testing the model for different airfoils

We now test the NN from the previous section, which was built on data from the NACA 63_3-418 airfoil, with the DU96-w-180, Risø B1-18, and Risø C2-18 airfoils, which are also part of the data set. All data for these airfoils are with the stall strip defect only. The DU96-w-180 and Risø C2-18 airfoils are designed with different goals from the NACA 63_3-418 and Risø B1-18 airfoils. The aerodynamics should be less sensitive to transition.

The number of cases tested and successfully detected by the NN are shown in Fig. 17. We see that the NN correctly predicts the defects to be stall strips with reasonable accuracy for the Risø B1-18 and Risø C2-18, but fails most of the time for the DU96-w-180. As this airfoil is significantly different from the training data, this is somewhat expected. The success for the Risø C2-18 is surprising.

The same heatmap analysis from before is shown for the airfoil cases in Fig. 18. The stall strip is the most often predicted defect type and the accuracy is similar to the previous section, albeit higher. Interestingly, the three stall strip lines in Fig. 18 and the stall strip line in Fig. 16 are all different, with different defects appearing more prominently for different lines.

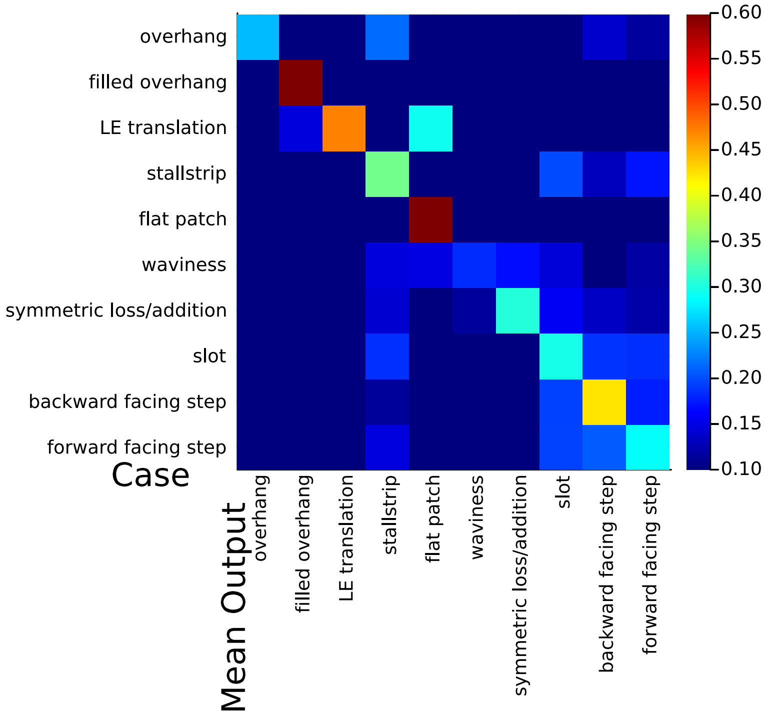

Figure 16: Mean probability the NN associates with each defect type for each defect type.

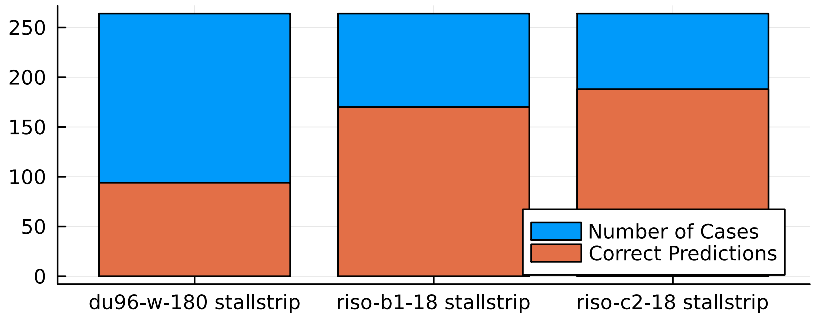

Figure 17: Number of cases and correct predictions using the NN, per defect type.

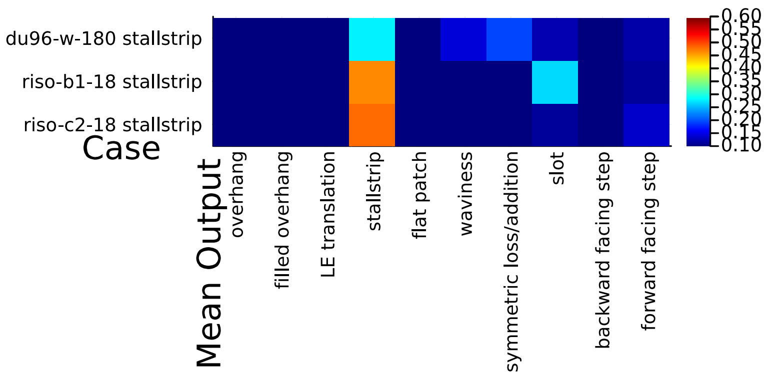

Figure 18: Mean probability the NN associates with each defect type for each defect type.

5.3 Reducing the number of defect categories

As we have consistently seen in the previous sections, the overhang, stall strip, slot, backward facing step, and forward facing steps are very similar, both geometrically and aerodynamically. These are all variations of localized steps in the geometry. Hence, we could combine them all into one defect type. Doing that would mean that the vast majority of our training data would fall into that single defect type. Hence, we instead remove the overhang, slot, and steps altogether and use the stall strip data instead.

We choose to preserve the waviness and remove the symmetric loss/addition. Both are defects that can affect both the suction and pressure sides of the airfoils, which depending on the dimensions can behave like a stall strip or have more extreme impacts on the aerodynamics.

We now repeat the process from before, training the NN on the data set for Re = [3, 5, 10] million and testing it for Re = 7 million. These results are shown in Fig. 19. We also test the NN on the different airfoils and results are shown in Fig. 20. The number of correct predictions is dramatically improved from the previous analysis, being correct well over 70% of the time, indicating that the defects have distinct aerodynamic behavior. The Risø B1-18 airfoil is correctly assessed almost every time. Filled overhang, LE translation, and stall strips are also very well captured. Waviness and flat patches are more difficult to distinguish from the other defect, but are still correctly categorized most of the time.

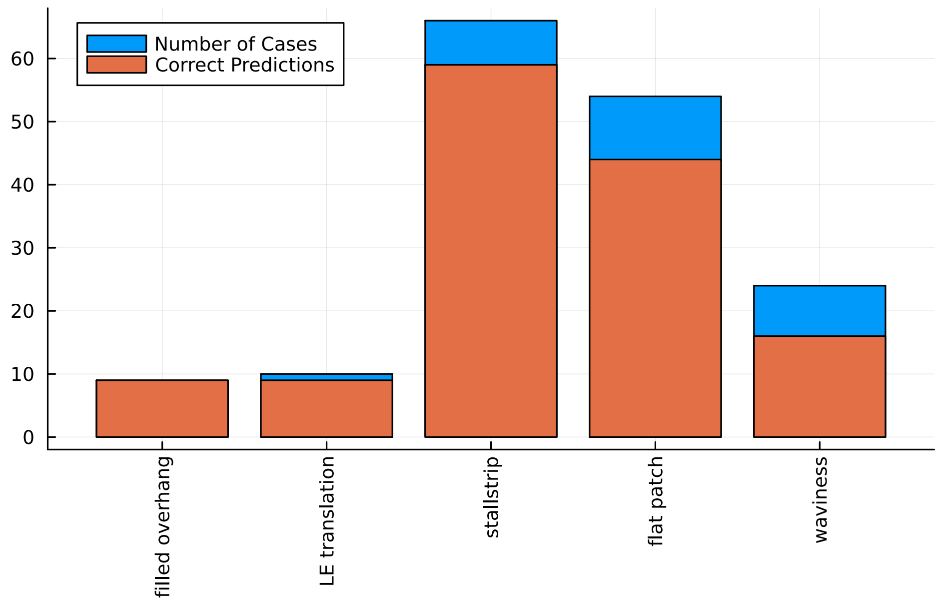

Figure 19: Number of cases and correct predictions using the NN, per defect type. Reynolds number case.

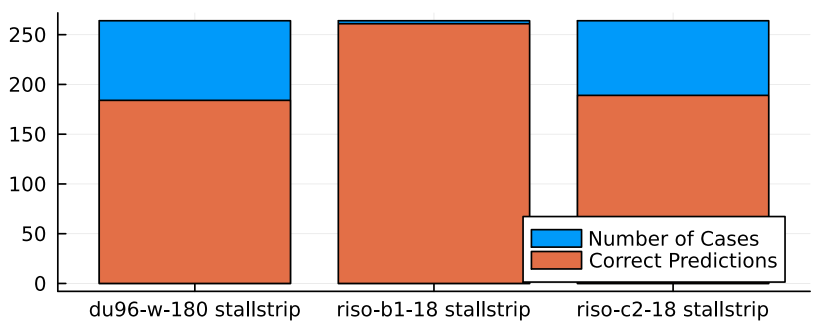

Figure 20: Number of cases and correct predictions using the NN, per defect type. Other airfoils case.

Fig. 21 shows the scatter plots for the aerodynamic parameters, now restricted to the reduced list of defect types and focusing on the parameters that ilustrate the differences best, for clarity and brevity.

Results are much more clustered than in Fig. 2. LE translation is clearly its own category, especially when observing at $\Delta\max(C_l/C_d)$ vs $\Delta C_l(\alpha=0°)$. Flat patch cases can be grouped with small stall strips that lead to small $\Delta\alpha@C_l=0$, which correspond to stall strips near $x/c=0$ (see Fig. 6), which is where the flat patch is most effective at disrupting the aerodynamics (see Fig. 7). Filled overhang cases can be grouped with stall strips that have $\Delta\max(C_l/C_d)=0$, which are cases where the stall strip is slightly towards the pressure side of the LE (see Fig. 6), where the filled overhang occurs. Looking at $\Delta\max(C_l/C_d)$ vs $\Delta C_l(\alpha=0°)$, the stall strip cases seem to fall within two major groups, one with higher values of $\Delta C_l(\alpha=0°)$, and one with lower values. The first are associated with stall strip positioned towards the suction side, while the latter is associated with cases where the stall strip is on the pressure side (see Fig. 6). Finally, waviness behaves like the stall strip, disturbing the sensitive region towards the suction side of the LE, but as the waviness amplitude increases, some aerodynamic parameters ($\Delta C_l(\alpha=0°)$, $\Delta\min(C_d)$) suddenly jump to more extreme ranges compared to the stall strip. This occurs when waviness becomes large enough to disturb the pressure side, as even modest values can disturb the suction side. The higher sensitivity to waviness on the suction side can be noticed in Fig. 14. Note from Fig. 2 that symmetric loss/addition can overlap with the waviness results, as it also affects both sides of the airfoil.

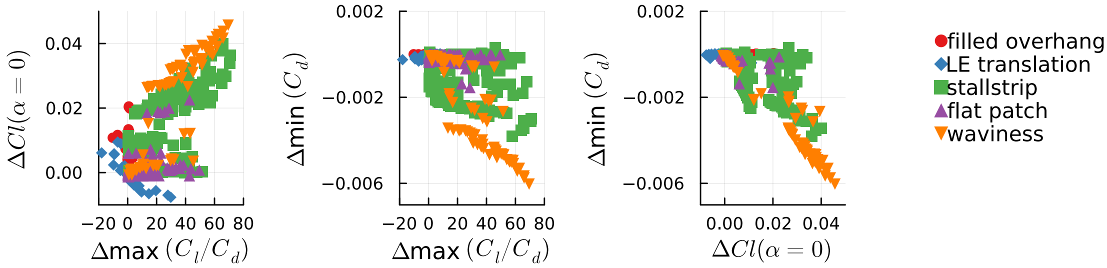

Figure 21: Scatter plots for all selected parameters, colored by defect type. Transitional cases only, $\mathrm{Re}=[3,5,10]$ million.

The data indicate that local defects could be classified in terms of their position relative to the LE, with defects at the LE behaving slightly different from defects towards the pressure or suction sides. This is only valid for surface quality defect types, with LE translation requiring its own category. Note also that the overhang can behave similar to a filled overhang at low values, but at large negative values it behaves more like a stall strip (see Figs. 2 and 3). Hence, barring special cases like LE translation, defects that cause disturbances to the boundary layer, like early transition and, in more extreme cases, separation, can be classified in terms of their location relative to the LE.

To verify the LE distance clustering hypothesis, we look at the scatter plots again in Fig. 22, where we now color the cases defined by a localized step (stall strip, slot, backward facing step, and forward facing step) by their distance to the LE. We can clearly see aligned sets of dark blue cases, furthest towards the suction side, and clusters of dark red cases, furthest to the pressure side, with the grey cases in between also showing grouping patterns. We also show the waviness and symmetric loss/addition in green, demonstrating that they can behave like more extreme cases of the suction side steps, as they disturb both sides of the airfoil.

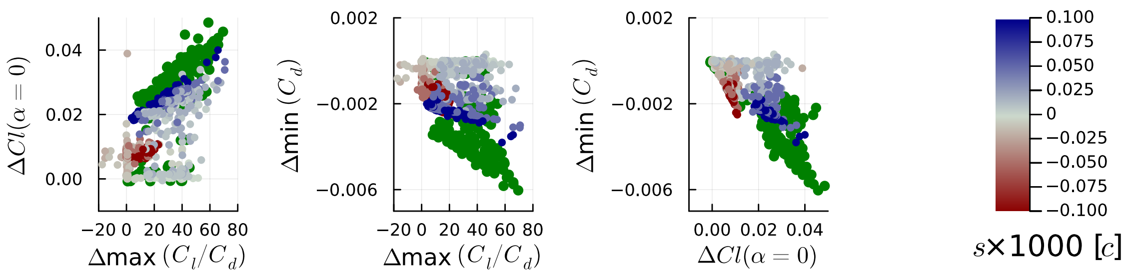

Figure 22: Scatter plots for stall strip, slot, backward facing step, and forward facing step, colored by distance to the LE, where blue is towards the suction side, red towards the pressure side, and white on the LE. Cases with defects on both sides, waviness and symmetric loss/addition, are in green. Transitional cases only, $\mathrm{Re}=[3,5,10]$ million.

6 Conclusions

Most LE defects included in this work serve as transition strips and have similar effects on aerodynamics, with the largest impact on C_l/C_d. Classifying LE defects based on their visual properties is less useful, from a power production point of view, than classifying them based on their aerodynamic effects.

From the original 11 defects in the data set analyzed here, we believe that from an aerodynamics point of view it is appropriate to group all defects with surface steps together. LE translation is clearly unique compared to the other defects, as it changes the airfoil camber. Grouping surface imperfections (e.g. steps) defects based on the distance from the LE (i.e., on the LE, towards the pressure side, towards the suction side, or on both sides of the LE) seems to be the most adequate way to categorize these defects under aerodynamic considerations. The height of the defects also plays a role and can be used to help establish the severity of the defect within a category.

From a blade maintenance point of view, identifying steps near the LE from photographs captured by drones is relatively simple. Then, by quantifying the distance from the LE, one could quickly estimate how aerodynamically meaningful the defect is.

Finally, from an operations point of view, the conclusion that LE erosion at the LE or on the pressure side is preferred over erosion on the suction side could lead to different approaches to how to handle above rated wind speeds. Pitching the blades to reduce the angle of attack would lead to enhanced erosion on the suction side, hence other options for lift control (e.g. the use of flaps) might have durability advantages. If negative angles of attack are unavoidable, especially during rain (instead of reducing the blade tip speed, applying leading edge protection on a larger extent of the blade suction side could be valuable in reducing maintenance costs.

The analysis conducted here was limited to the numerically generated LE defects data set and different defect types or more extreme dimensions of the defects could lead to different conclusions. Future work could focus on extending the analysis to larger data sets, including experimental sources. Another limitation of the current work is that the defects investigated were obtained from 2D simulations. In real blades, erosion often happens near the tips, where 3D effects can play a role. The differences between LE defects in 2D airfoils and blade tips could be a topic for future studies.

Acknowledgments

DTU's contribution to this work was financed through the LERCat project funded by the Danish Energy Council (EUDP-64021-2027).

References

[1] Agrim Sareen, Chinmay A. Sapre, and Michael S. Selig. Effects of leading edge erosion on wind turbine blade performance. *Wind Energy*, 17(10):1531–1542, 2014.
[2] Christopher M. Langel, Raymond C. Chow, C. P. van Dam, and David Charles Maniaci. Rans based methodology for predicting the influence of leading edge erosion on airfoil performance. 10 2017.
[3] David Maniaci, Carsten Westergaard, Alan Hsieh, and Joshua Paquette. Uncertainty quantification of leading edge erosion impacts on wind turbine performance. *Journal of Physics: Conference Series*, 1618:052082, 09 2020.
[4] Leon Mishnaevsky, Charlotte Bay Hasager, Christian Bak, Anna-Maria Tilg, Jakob I. Bech, Saeed Doagou Rad, and Søren Fæster. Leading edge erosion of wind turbine blades: Understanding, prevention and protection. *Renewable Energy*, 169:953–969, 2021.
[5] Leon Mishnaevsky, Antonios Tempelis, Nikesh Kuthe, and Puneet Mahajan. Recent developments in the protection of wind turbine blades against leading edge erosion: Materials solutions and predictive modelling. *Renewable Energy*, 215:118966, 2023.
[6] Javier Contreras López, Athanasios Kolios, Lin Wang, and Manuel Chiachio. A wind turbine blade leading edge rain erosion computational framework. *Renewable Energy*, 203:131–141, 2023.
[7] J. I. Bech, C. B. Hasager, and C. Bak. Extending the life of wind turbine blade leading edges by reducing the tip speed during extreme precipitation events. *Wind Energy Science*, 3(2):729–748, 2018.
[8] A. F. P. Ribeiro. Unsteady RANS modelling of flow past a rectangular 5:1 cylinder: investigation of edge sharpness effects. *13th International Conference on Wind Engineering*, 2011.

[9] Robert S Ehrmann, Benjamin Wilcox, Edward B White, and David Charles Maniaci. Effect of surface roughness on wind turbine performance, 2017.

[10] Geza Schrauf. On allowable surface tolerances for laminar flow, June 2022.

[11] Alexander Meyer Forsting, Anders S. Olsen, Niels N. Sørensen, and Christian Bak. The impact of leading edge damage and repair on sectional aerodynamic performance. *AIAA SCITECH Forum*, 2023.

[12] Alexander Meyer Forsting and Niels N. Sørensen. Leading edge roughness and repair CFD dataset. 12 2022.

[13] Simon Haykin. *Neural networks: a comprehensive foundation*. Prentice Hall PTR, 1998.

[14] Tobias Knopp, Bernhard Eisfeld, and Javier Bartolome Calvo. A new extension for k–ω turbulence models to account for wall roughness. *International Journal of Heat and Fluid Flow*, 30(1):54–65, 2009.

[15] A. F. P. Ribeiro, A. M. Awruch, and H. M. Gomes. An airfoil optimization technique for wind turbines. *Applied Mathematical Modelling*, 36(10):4898–4907, 2012.

[16] M. Richmond, A. Sobey, R. Pandit, and A. Kolios. Stochastic assessment of aerodynamics within offshore wind farms based on machine-learning. *Renewable Energy*, 161:650–661, 2020.

[17] Lorenzo Cappugi, Alessio Castorrini, Aldo Bonfiglioli, Edmondo Minisci, and M. Sergio Campobasso. Machine learning-enabled prediction of wind turbine energy yield losses due to general blade leading edge erosion. *Energy Conversion and Management*, 245:114567, 2021.